

Optically thick H_I dominant in the local interstellar medium; an alternative interpretation to “dark gas”¹

Y. Fukui², K. Torii², T. Onishi³, H. Yamamoto², R. Okamoto², T. Hayakawa², K.
Tachihara², and H. Sano²

²Department of Physics, Nagoya University, Chikusa-ku, Nagoya, Aichi 464-8601, Japan

³Department of Astrophysics, Graduate School of Science, Osaka Prefecture University, 1-1
Gakuen-cho, Nakaku, Sakai, Osaka 599-8531, Japan

fukui@a.phys.nagoya-u.ac.jp

Received _____; accepted _____

ABSTRACT

Dark gas in the interstellar medium (ISM) is believed to not be detectable either in CO or HI radio emission, but it is detected by other means including γ -rays, dust emission and extinction traced outside the Galactic plane at $|b| > 5^\circ$. In these analyses, the 21-cm HI emission is usually assumed to be completely optically thin. We have reanalyzed the HI emission from the whole sky at $|b| > 15^\circ$ by considering temperature stratification in the ISM inferred from the *Planck/IRAS* analysis of the dust properties. The results indicate that the HI emission is saturated with an optical depth ranging from 0.5 to 3 for 85 % of the local HI gas. This optically thick HI is characterized by spin temperature in the range 10 K–60 K, significantly lower than previously postulated in the literature, whereas such low temperature is consistent with emission/absorption measurements of the cool HI toward radio continuum sources. The distribution and the column density of the HI are consistent with those of the dark gas suggested by γ -rays, and it is possible that the dark gas in the Galaxy is dominated by optically thick cold HI gas. This result implies that the average density of HI is 2–2.5 times higher than that derived on the optically-thin assumption in the local ISM.

Subject headings: ISM: clouds — radiolines: ISM

1. Introduction

It is important to quantify the constituents of the interstellar medium (ISM), which mainly consists of neutral, molecular and ionized hydrogen HI, H₂, and HII, in order to understand the role of the ISM in galactic evolution. The HI gas has density mainly in a range from 0.01 cm⁻³ to 100 cm⁻³ while the CO probes the molecular hydrogen gas at density higher than 1000 cm⁻³, so the intermediate density regime 100 cm⁻³ – 1000 cm⁻³ may possibly remain unrecognized. It has been discussed that “dark gas” may exist, which is undetectable in radio emission, either in the 21-cm HI or 2.6-mm CO transitions (Grenier et al. 2005; *Planck* Collaboration et al. 2011). Previous studies suggest that the dark gas probed by γ -rays and dust emission has a density regime between the HI and H₂ as inferred from its spatial distribution intermediate between HI and CO (Grenier et al. 2005; *Planck* Collaboration et al. 2011).

The physical properties of the CO emitting molecular gas are relatively well understood due to transitions of its different rotational states and isotopic species, which allow us to derive physical and chemical parameters of the CO gas. On the other hand, the physical parameters of the HI gas are more difficult to estimate, because the HI line intensity is the only measurable quantity for a combination of two unknown parameters, the spin temperature T_s and optical depth τ_{HI} . The 21-cm transition is a transition characterized by the excitation temperature, called spin temperature, between the two spin-flip states in the electronic ground state. The HI consists of warm neutral medium (WNM) and cold neutral medium (CNM; for a review see Dickey & Lockman 1990; Kalberla & Kerp 2009). The mass of the HI gas is measurable at reasonably high accuracy under the optically

¹Based on observations obtained with *Planck* (<http://www.esa.int/Planck>), an ESA science mission with instruments and contributions directly funded by ESA Member States, NASA, and Canada.

thin approximation, while the cold components having T_s of ≤ 80 K may not be easily measurable because of optical depth effects. Only a comparison of the absorption and emission HI profiles toward extragalactic radio continuum sources can be used to estimate T_s and τ_{HI} (Dickey et al. 2003; Heiles & Troland 2003b), so the details of the cold HI are still not fully understood. The existence of optically thick HI in galaxies has been discussed based on line profiles, whereas a quantitative method to evaluate the physical properties has not yet been developed (Braun 2012).

A recent work on the high latitude molecular clouds MBM 53, 54, 55, and HLCG 92-35 has shown that the HI emission is optically thick in the surroundings of the CO clouds (Fukui et al. 2014, Paper I). These authors compared the *Planck/IRAS* dust opacity (Planck Collaboration et al. 2014a) with HI and CO, and estimated T_s to be 20 K–40 K (average is 30 K) and τ_{HI} 0.3–5 (average is 2) by assuming that the dust opacity is proportional to the ISM proton column density. They suggest that the HI envelope is massive having more than 10 times the mass of the CO clouds, and that such optically thick HI may explain the origin of the dark gas, an alternative to CO-free H_2 . It is important to test if the HI shows similar high optical depth in a much larger portion of the sky.

In addition, it is notable that in three TeV γ -ray supernova remnants RX J1713.7-3946, RX J0852.0-4622, and HESS J1731-347, it is found that spatially extended cold HI gas of $T_s \sim 40$ K which has no CO emission is responsible for the γ -rays via the hadronic process between the cosmic-ray protons and the interstellar protons (Fukui et al. 2012; Torii et al. 2012; Fukui 2013; Fukuda et al. 2014). The cold HI probably represents the compressed HI shell swept up by the stellar winds of the supernova progenitor. This finding raised independently a possibility that the cold HI gas may be more ubiquitous than previously thought.

It has been difficult to derive T_s and τ_{HI} in general and our knowledge on the cold HI

remains ambiguous at best. In order to better understand the relationship between the dust emission and HI over a significant portion of the sky, we have compared the HI with the dust properties derived from the *Planck* and *IRAS* data beyond the area studied by Paper I. This comparison was made by using the HI dataset at 33′ resolution from the Leiden/Argentine/Bonn (LAB) archive data and the *Planck/IRAS* dust properties. We present the results of the detailed comparison. Section 2 presents the observations, Section 3 the results, Section 4 the discussion and Section 5 our conclusions.

2. Observational Datasets

2.1. Datasets

In this study we used the all sky maps of the dust model data measured by *Planck/IRAS*, the LAB HI data, the CfA CO data, 1.4 GHz radio continuum data, and H α data. All the datasets are smoothed to be a HPBW of 33′, which corresponds to the HPBW of the LAB HI data, and are then converted into the Mollweide projection with a grid spacing of 30′.

2.1.1. HI Data

The LAB HI 21-cm survey (Kalberla et al. 2005) is used in this study. It covers the entire sky at an effective angular resolution of 33′ (HPBW). The data is taken from the web page of the LAMBDA project⁴ with Healpix format⁵. The rms noise fluctuations of the HI data are 0.07 K–0.09 K in T_{mb} at 1 km s^{−1} velocity resolution (Kalberla et al. 2005).

⁴<http://lambda.gsfc.nasa.gov>

⁵<http://healpix.jpl.nasa.gov>

The effective velocity range of the present analysis is $\sim \pm 10 \text{ km s}^{-1}$ in v_{LSR} where the HI is peaked at around 0 km s^{-1} , while the HI integrated intensity W_{HI} is calculated using a radial velocity, v_{LSR} , range from -150 km s^{-1} to $+150 \text{ km s}^{-1}$. More details on the velocity range are given in Section 2.2.

2.1.2. *Planck/IRAS Data*

Archival datasets of dust optical depth at 353 GHz, τ_{353} , and dust temperature, T_{d} , are used to make comparisons with the HI data, where the 353, 545 and 857 GHz data of the first 15 months observations with *Planck* and the $100 \mu\text{m}$ data obtained with *IRAS* are used to derive τ_{353} and T_{d} (see Planck Collaboration et al. 2014a, for details). Here we utilize version R1.20 of the *Planck* maps.

2.1.3. *CO Data*

We use the integrated intensity $^{12}\text{CO } J=1-0$ map over the full observed velocity range by Dame et al. (2001) as a molecular gas tracer. The HPBW is $8.7'$, and the rms noise fluctuations are $0.1 \text{ K} - 0.35 \text{ K}$ at 1.3 km s^{-1} velocity resolution (Dame et al. 2001). The data are also taken from the LAMBDA project page.

2.1.4. *Background 21-cm Continuum Data*

The 21-cm continuum emission is used as background emission of HI. We use the CHIPASS 21-cm radio continuum map with a sensitivity of $\sim 40 \text{ mK}$ (Calabretta et al. 2014) for the southern sky and the Stockert 21-cm radio continuum map with a sensitivity of $\sim 50 \text{ mK}$ (Reich & Reich 1986) for the northern sky. The original HPBWs are $14.4'$ and $35'$,

respectively. This continuum emission includes the cosmic microwave background emission.

2.1.5. $H\alpha$ Data

In order to mask the region where dust is locally heated or destroyed by ultraviolet (UV) radiation, we use the all-sky $H\alpha$ data provided by Finkbeiner (2003). The angular resolution is $6'$. Typical uncertainties in each pixel is estimated to be 0.3–1.3 Rayleigh for $|b| > 15^\circ$ and 1–5 Rayleigh for $|b| \leq 15^\circ$.

2.2. Masking

Figure 1 shows the distribution of τ_{353} , which includes mainly local clouds like Taurus, Lupus, Aquila, Polaris flare and Chameleon within 200 pc of the Sun. A correlation analysis between dust and gas must be done toward a single component of the ISM and regions that do not overlap along the line of sight are chosen for comparison. Otherwise, regions of different physical properties will be mixed up, reducing the correlation among the physical parameters. It is also important to avoid contamination so that local irradiation by high-mass stars does not significantly affect the dust emission. Considering these, we selected the region for the present analysis according to the following five criteria.

1. The Galactic latitude $|b|$ is higher than 15° in order to eliminate contamination by different components in the Galactic plane along the line of sight. At intermediate latitudes the assumption that the ISM emission in any given direction is dominated by a single structure (cloud or cloud complex) is a valid approximation over most of the sky. This approximation ignores the very diffuse gas (inter-cloud medium) that is present at some level in all directions. At high latitudes the diffuse gas (neutral and ionized) is sometimes the only form of interstellar matter on the line of sight, with

column density below about 10^{20} cm^{-2} . There is no evidence for “dark gas” at these low column densities, so we ignore the diffuse gas in this analysis.

2. Extragalactic objects such as the LMC, SMC and M31 are removed from the present analysis. The points where W_{HI} at $|v_{\text{LSR}}| > 100 \text{ km s}^{-1}$ are larger than 10 % of those at $|v_{\text{LSR}}| < 70 \text{ km s}^{-1}$ are masked. In addition, the low velocity component of the Magellanic stream seen at $l \sim -60^\circ - +60^\circ$ and $b < -60^\circ$ is masked by hand using the integrated intensity map at $|v_{\text{LSR}}| < 70 \text{ km s}^{-1}$ to show a continuous distribution with the components seen at $|v_{\text{LSR}}| > 70 \text{ km s}^{-1}$.
3. As seen in the HI longitude-velocity map in Figure 2(a), the HI components are concentrated around $|v_{\text{LSR}}| < 30 \text{ km s}^{-1}$. We thus remove the points that have HI emission from -70 km s^{-1} to -35 km s^{-1} , those are identified as the intermediate velocity clouds mainly distributed at $60^\circ < b < 80^\circ$ (Planck Collaboration et al. 2011, 2014a). The points where W_{HI} are larger than 50 K km s^{-1} at $35 \text{ km s}^{-1} < |v_{\text{LSR}}| < 70 \text{ km s}^{-1}$ are masked.
4. In order to eliminate locally heated components, the $\text{H}\alpha$ emission is restricted to be weaker than 5 Rayleigh (Finkbeiner 2003). This eliminates the dust in ionized regions (e.g., in Orion A, the Ophiuchus region, etc.), where the dust may be destroyed or heated by the UV photons, causing an anomalous dust to gas ratio and dust temperature.
5. CO gas has a different physical environment with higher density. Regions with detectable CO emission with integrated intensities of larger than 1 K km s^{-1} are excluded by using the CO data provided by Dame et al. (2001). Individual regions of CO gas not included in the present study will be dealt with in detail at higher resolution in separate papers.

The entire masked region is shown in Figure 1, and Figure 2(a) shows the longitude-velocity map after masking by criteria 1, 2, 4 and 5, and Figure 2(b) by all the criteria including the criterion 3. Figure 3 also shows the histograms of the peak velocities and 1σ velocity dispersions, σ_v , for the resulting HI data. The present analysis substantially excludes, by masking, components that are broad and separated by more than 35 km s^{-1} from the main HI emission at around 0 km s^{-1} (Figure 3). The fraction of W_{HI} of v_{LSR} between -9 km s^{-1} and $+6\text{ km s}^{-1}$ accounts for 86 % (Figure 3(a)) and that having σ_v less than 10 km s^{-1} is 81 % (Figure 3(b)), while we otherwise estimate W_{HI} by using a v_{LSR} range from -150 km s^{-1} to $+150\text{ km s}^{-1}$. The main HI component corresponds to velocities showing CNM in general. On the other hand, the major part of the WNM has large linewidth of more than 20 km s^{-1} and a peak velocity often shifted by more than 10 km s^{-1} from the main HI peak (Heiles & Troland 2003a). A single T_s for the present substantially narrow velocity range is a reasonable assumption as a first-order approximation, and is consistent with the results in the high-latitude clouds (Paper I).

3. Results

3.1. τ_{353} Versus N_{HI}

Figure 4(a) shows a scatter plot between W_{HI} and τ_{353} for the entire region analyzed. This plot has a correlation coefficient of 0.79. In the same manner in Paper I, in order to see the dependence on T_d , we colored the data points in a window of 0.5 K in T_d every 1 K in Figures 4(b) and 4(c). We see clearly that points for each T_d show better correlation with a correlation coefficient higher than 0.9. We obtained best-fit straight regression lines by least-squares fitting (Table 1). Here, for the ranges $22.0\text{ K} \leq T_d < 22.5\text{ K}$ and $22.5\text{ K} \leq T_d$, the number of points is less than for the other ranges, and we thus assume that the intercept is zero and make fits only for slopes. The regression shows a trend that

the slope of W_{HI} with respect to τ_{353} becomes smaller systematically with decreasing T_{d} . This trend is similar to what is found in the case of high-latitude clouds (Paper I). Recent studies by the *Planck* Collaboration have also found that T_{d} increases with decreasing gas column density (Planck Collaboration et al. 2014a,b). By following the same argument as in Paper I, we expect that the HI emission is moderately optically thick in general and that the saturation due to the optical depth effect causes weaker W_{HI} for lower T_{d} and higher τ_{353} . The optically thin limit is seen only for the highest T_{d} , and the rest of the points with lower T_{d} and shallower slopes suffer from saturation in HI intensity. We apply the optically thin relationship in equation (1) in order to convert W_{HI} into the HI column density under the optically thin approximation N_{HI}^* ,

$$N_{\text{HI}}^* [\text{cm}^{-2}] = 1.823 \times 10^{18} \cdot W_{\text{HI}} [\text{K km s}^{-1}], \quad (1)$$

With the optically thin points at $22.5 \text{ K} \leq T_{\text{d}}$ in Figures 4(b) and (c), we obtain a relationship between W_{HI} and τ_{353}

$$W_{\text{HI}} [\text{K km s}^{-1}] = k \cdot \tau_{353}, \quad (2)$$

where $k = 1.15 \times 10^8 \text{ K km s}^{-1}$ is a constant. This relation will hold for any optically thin values of τ_{353} , even if the HI emission is not optically thin, as long as the dust properties are uniform with no significant spatial variation. We tested the variation of k as a function of b and find that the peak-to-peak dispersion of k is less than 10 % for $|b| = 50^\circ - 90^\circ$. Finally using equations (1) and (2), we can convert τ_{353} into the HI column density, N_{HI} , by the following equation,

$$\frac{N_{\text{HI}} [\text{cm}^{-2}]}{N_0} = \frac{\tau_{353}}{\tau_0}, \quad (3)$$

where $N_0 = 1 \times 10^{21} \text{ cm}^{-2}$ and $\tau_0 = 4.77 \times 10^{-6}$ are typical values for intermediate latitude lines of sight (see Section 3.2 and Figure 9 below).

3.2. Temperature-dependent Analysis of HI

The above results suggest that the HI emission is partially saturated due to the optical depth effect for lower temperatures and the degree of saturation depends on T_s of the HI in a way similar to the high-latitude clouds (Paper I). W_{HI} is expressed by a radiation transfer equation

$$W_{\text{HI}} [\text{K km s}^{-1}] = (T_s [\text{K}] - T_{\text{bg}} [\text{K}]) \cdot \Delta V_{\text{HI}} [\text{km s}^{-1}] \cdot [1 - \exp(-\tau_{\text{HI}})], \quad (4)$$

where T_s is assumed to be uniform on the line of sight, T_{bg} is the background radio continuum radiation, and ΔV_{HI} is the HI linewidth ($\Delta V_{\text{HI}} = W_{\text{HI}}/T_{\text{peak}}$ for single-component spectra, where T_{peak} is the peak temperature of the HI emission at each point). Equation 4 makes the assumption that all the HI in each velocity channel is at a single temperature, and τ_{HI} is the average in ΔV_{HI} .

By assuming that τ_{353} is solely ascribed to the dust in the HI gas, we are able to estimate T_s and τ_{HI} . This assumption needs to be examined because molecular hydrogen with no detectable CO may account for some fraction of the total column density, N_{H} , at space density, n_{H} above 100 cm^{-3} . It is also worth considering whether the spatial variation of dust properties may offer an alternative explanation. We shall discuss these possibilities later in Section 4.

Under the present assumption, τ_{353} is converted into N_{HI} by equation (3) or $N_{\text{HI}} [\text{cm}^{-2}] = 2.1 \times 10^{26} \cdot \tau_{353}$, and W_{HI} into N_{HI}^* by equation (2). N_{HI}^* gives an underestimate of the actual N_{HI} if the HI emission is not optically thin, and the ratio $N_{\text{HI}}/N_{\text{HI}}^*$ is given as

$$N_{\text{HI}}/N_{\text{HI}}^* = \tau_{\text{HI}}/[1 - \exp(-\tau_{\text{HI}})], \quad (5)$$

where τ_{HI} is given by the following equation which is valid for any positive optical depth;

$$\tau_{\text{HI}} = \frac{N_{\text{HI}} [\text{K km s}^{-1}]}{1.823 \times 10^{18}} \cdot \frac{1}{T_s [\text{K}]} \cdot \frac{1}{\Delta V_{\text{HI}} [\text{km s}^{-1}]} \quad (6)$$

Figure 5 shows a curve of equation (5).

Along with the assumption that there is only one cloud structure that dominates the emission by dust and gas on any given line of sight, we further assume that there is a single T_s for the HI gas in this structure. Relaxing this assumption to include warm and cool gas phases associated with the cloud would make equations (4) and (6) more complicated, and introduce more unknown quantities into the analysis. For the present paper, we keep the analysis simple by assuming that a single spin temperature dominates the HI on each line of sight.

We here solve the two coupled equations (4) and (6) to estimate T_s and τ_{HI} . Note that these two equations are independent as long as τ_{HI} is finite, although they become essentially a single equation in the optically thin limit. Discussion of optically thick HI is also found in the literature (Strasser & Taylor 2004; Dickey 2013). Examples for T_s and τ_{HI} determination are shown in Figure 6, with the results summarized in Table 2. Figure 7 shows the distributions of T_s , τ_{HI} and N_{HI} colored by their fractional errors. Here we estimate the error in T_s and τ_{HI} as shown by thick lines in Figure 6 from the 1σ uncertainties of τ_{353} and W_{HI} . The error in N_{HI} is also calculated using equation (3) from the error in τ_{353} . It is shown that the method cannot be applied with high accuracy when τ_{HI} is smaller than ~ 0.2 because of the degeneracy of equations (4) and (6). We therefore excluded the regions where τ_{HI} is smaller than 0.2. Figure 7(c) indicates that N_{HI} is accurately determined within $\pm 5\%$, while the errors in T_s and τ_{HI} are not always small.

The spatial distributions of the derived T_s , τ_{HI} and N_{HI} are shown in Figure 8, and Figure 9 shows histograms of these three parameters. In Figures 8(a) and (b) the points with $\tau_{\text{HI}} < 0.2$ are shown in white, and we use N_{HI}^* instead of N_{HI} for these points in

Figure 8(c), while these points are not included in Figure 9. The mass ratio of the points with $\tau_{\text{HI}} < 0.2$ to all the data points is only 3 %. As seen in Figure 9, τ_{HI} ranges from 0.5 to 3.0 for 85 % of the total HI gas, where the HI gas with τ_{HI} larger than 0.5 accounts for 91 %. On the other hand, T_s ranges from 15 K to 35 K for 78 % and T_s is less than 35 K for 84 %. N_{HI} ranges from $5 \times 10^{20} \text{ cm}^{-2}$ to $3 \times 10^{21} \text{ cm}^{-2}$ for 73 %, where the peak is seen at 10^{21} cm^{-2} .

There has been discussion that T_s is generally higher than 80 K, with 130 K as the nominal value in the literature (e.g., Mohan et al. 2004). On the other hand, Dickey et al. (2003) and Heiles & Troland (2003b) showed that there exists cold HI gas (CNM) having T_s of 20 K–50 K from HI emission/absorption profiles toward radio continuum background sources. This T_s range is consistent with the current T_s distribution.

The observed W_{HI} as a function of the computed N_{HI} from equation (3) with colors showing the value of $T_s = 10 \text{ K} - 100 \text{ K}$ is shown in Figure 10. Generally, W_{HI} begins to saturate at HI optical depth around 0.3. For lower T_s , saturation begins at lower N_{HI} , and for higher T_s the correlation between W_{HI} and N_{HI} becomes better than for lower T_s . Since both T_s and T_d are determined by radiative heating and cooling (see Section 4 in Paper I), the qualitative trend of the T_d -dependence of W_{HI} should be consistent with that found in Figure 4.

We shall estimate the total ISM mass in the solar vicinity in the unmasked area. The HI masses with optical-depth correction and that without correction are $1.0 \times 10^6 M_\odot$ and $0.5 \times 10^6 M_\odot$, respectively, for an assumed distance of 150 pc (Paper I). This implies the mass increase due to the optical depth correction amounts to $0.5 \times 10^6 M_\odot$, or a factor of ~ 2.0 , similar to the high-latitude clouds in Paper I. We also estimate the total ISM mass for the entire sky including the masked area by extrapolating τ_{353} and W_{HI} . In Figure 11 we show the latitude distribution of τ_{353} and W_{HI} averaged in Galactic longitude, where

the two curves, dashed and solid lines, indicate the entire area with and without masking, respectively. We fit the data by tentatively assuming a Lorentzian function as shown in Figure 11 to estimate the mass in the masked area. The estimated total masses with N_{HI} and N_{HI}^* are $2.9 \times 10^6 M_{\odot}$ and $1.2 \times 10^6 M_{\odot}$, respectively, suggesting the optical depth correction amounts of $1.7 \times 10^6 M_{\odot}$, or a factor of 2.5.

4. Discussion: Ubiquitous optically-thick HI, an alternative explanation for the dark gas

The optically thick HI gas has been identified in the region of MBM 53, 54, 55 and HLCG 92-35, and the CO clouds are enveloped by massive HI gas having more than 10 times greater mass than the CO clouds (Paper I). The present study has shown that optically-thick HI is common in interstellar space within 200 pc of the Sun. The typical parameters of the HI gas ($\geq 70\%$ of the total) are summarized as follows; $T_s = 15 \text{ K} - 35 \text{ K}$, $\tau_{\text{HI}} = 0.5 - 3.0$, and $N_{\text{HI}} = 5 \times 10^{20} \text{ cm}^{-2} - 3 \times 10^{21} \text{ cm}^{-2}$ (Figure 9). If we tentatively assume a typical line-of-sight depth of 5 pc for the cold HI, the average density is estimated to be $30 \text{ cm}^{-3} - 190 \text{ cm}^{-3}$. The ratio of the actual HI column density N_{HI} to that obtained under the optically thin approximation N_{HI}^* is estimated to be 2.0 over the region analyzed. The high density and low temperature of the cold HI gas are consistent with the temperature estimates in a model spherical cloud with the density range concerned, which is under heating by the interstellar radiation field and cooling by the atomic lines including CII (Goldsmith et al. 2007).

Grenier et al. (2005) presented the dark gas based on γ -ray observations by EGRET, which is not “detectable” either by HI or CO emission. Subsequently, *Planck* Collaboration et al. (2011) discussed that the dust emission includes the dark gas component which has a similar distribution to the excess γ -rays. Dark gas is also seen in

visual extinction (Paradis et al. 2012). According to these studies, the distribution of the dark gas is largely similar to the CO gas, but it is spatially extended beyond the limit of CO detection. Its correlation with the HI gas distribution did not seem to be strong in these previous studies that assumed optically thin HI. The present analysis has shown that the HI gas is dominated by an optically thick component. The typical HI column density derived for the optically thick case, $\sim 10^{21} \text{ cm}^{-2}$, is consistent with that of the dark gas (Grenier et al. 2005). Figures 12 and 13 show $N_{\text{HI}} - N_{\text{HI}}^*$ and $N_{\text{HI}}/N_{\text{HI}}^*$ at $33'$ resolution over the entire sky. These distributions are fairly similar to the dark gas distribution presented in Grenier et al. (2005) and *Planck* Collaboration et al. (2011). More quantitative comparison between the optically thick HI and γ -rays is a subject of a forthcoming paper.

For more details, in Figure 14 we show the scatter plot between N_{HI}^* and τ_{353} , similar to Figure 6 in *Planck* Collaboration et al. (2011). Figures 14(a)–(c) show the relationship between τ_{353} and N_{HI}^* with colors indicating the dependence of the relationship on τ_{HI} , T_s , and T_d , respectively. These figures indicate that the apparent scatter in the plot reflects the difference in temperature (T_d or T_s) or τ_{HI} , and that the actual scatter is much smaller than that in the $N_{\text{HI}}^* - \tau_{353}$ correlation (Figure 14). According to the present analysis, τ_{HI} takes maximum values of around 6–7 at $N_{\text{HI}}^* \sim 10^{21} \text{ cm}^{-2}$ or $W_{\text{HI}} \sim 550 \text{ K km s}^{-1}$, and this optical depth effect causes the apparent bump at $N_{\text{HI}}^* = 4 \times 10^{20} \text{ cm}^{-2} - 2 \times 10^{21} \text{ cm}^{-2}$ with a maximum at $N_{\text{HI}}^* \cong 9 \times 10^{20} \text{ cm}^{-2}$ as seen in Figure 14. The bump in the scatter plot is then interpreted in terms of the optical depth effect but not by the enhanced dispersion in the plot. We note that the bump is a natural outcome of the saturation effect in the optically thick HI with no ad-hoc assumption, whereas it was ascribed to the property of the unknown dark gas in the previous interpretation (*Planck* Collaboration et al. 2011). Figure 15 shows the correlation between the optical depth corrected HI column density N_{HI} and τ_{353} . Naturally, the scatter is small, on the order of 10 % at maximum in Figure 14(c). We consider that Figure 15 shows the real correlation with much smaller errors between

N_{HI} and τ_{353} .

In Figure 14(c) we find that the points below the optically thin limit in a range of N_{HI}^* of $7 \times 10^{19} \text{ cm}^{-2} - 5 \times 10^{20} \text{ cm}^{-2}$ are outside the regime where the present method has a solution. Most of these points are located at very high Galactic latitude higher than 60° as shown by black dots in Figures 8(a) and (b), where τ_{353} in the sky is very low (like 10^{-6}), and are characterized by the highest T_{d} of larger than 23 K; a typical point has $W_{\text{HI}} \sim 80 \text{ K km s}^{-1}$ and $\tau_{353} \sim 7 \times 10^{-7}$. We suggest that the coefficient k around 10^8 K km s^{-1} in equation (2) is larger in the higher b (greater than 60°) than in the lower b (less than 60°). If we adopt $k = 1.5 \times 10^8 \text{ K km s}^{-1}$ for instance, 99.7% of all the data points are explained in the present scheme (Figure 14). This condition will be fulfilled if the dust optical depth is smaller by $\sim 30\%$ at such low column density. Such a trend is qualitatively consistent with smaller dust grains in the extremely low column density condition and is worth further study.

In order to evaluate the effect of the dust opacity which may depend on hydrogen column density, we shall test the following equation (7) instead of equation (3);

$$\left(\frac{N_{\text{HI}} [\text{cm}^{-2}]}{N_0} \right)^{1.28} = \frac{\tau_{353}}{\tau_0}. \quad (7)$$

This relation is derived by assuming the dependence of sub-mm dust optical depth which is proportional to $N_{\text{HI}}^{0.28}$ for the total hydrogen column density N_{HI} above 10^{22} cm^{-2} in Orion A (Roy et al. 2013). A trend of dust opacity evolution with column density is also recognized for clouds with column density of $(3-7) \times 10^{21} \text{ cm}^{-2}$ in the Vela Molecular Ridge (Martin et al. 2012) and in the Taurus filaments (Ysard et al. 2013). We made the same analysis of the cold HI by using equation (7) instead of equation (3) and have naturally found similar results to those above with some minor changes of physical quantities. Equation (7) can alter N_{HI} by $-20\% - +30\%$ at a typical range $5 \times 10^{20} \text{ cm}^{-2} - 3 \times 10^{21} \text{ cm}^{-2}$ as

compared with the uniform dust opacity assumption, and the increase of the total HI mass due to the HI optical depth effect becomes slightly less by a factor of 2.1 instead of 2.0 for the unmasked area and 2.2 instead of 2.5 for the entire sky including the masked area (see Section 3.2). So it is not necessary to make a substantial change in the parameters of the cold HI, even when the possibility of non-uniform dust opacity is taken into account. Equation (7) also suggests that the dust opacity variation is not the major cause of the observed poor correlation in Figure 4(a). If the dust opacity variation is assumed to be substantial, the dust cross section must be increased to more than 300 % for $\tau_{\text{HI}} = 3$, which is not consistent with equation (7).

The present analysis has shown that cold HI is a viable interpretation of the dark gas. It, however, does not exclude the possibility that H_2 is dominant instead of HI in the dark gas. In order to explain the dark-gas origin, a possibility of molecular hydrogen with no CO emission has been discussed (e.g., *Planck* Collaboration et al. 2011). We here make a comparison with the results of direct UV absorption measurements of H_2 by FUSE and Copernicus (Gillmon et al. 2006; Rachford et al. 2002, 2009). They observed about 80 lines of sight toward active galactic nuclei and galactic OB stars, and 21 of them are included in the present analysis. The 21 sources are taken from Gillmon et al. (2006) and Rachford et al. (2002), and are summarized in Table 3. The H_2 abundance ratio is estimated by these authors as

$$f_{\text{H}_2}^* = \frac{2N_{\text{H}_2}}{2N_{\text{H}_2} + N_{\text{HI}}^*}, \quad (8)$$

where N_{H_2} is the column density of H_2 , and N_{HI}^* the HI column density. It is to be noted that the N_{HI}^* in Table 3 is derived under optically thin approximation measured with the 21-cm observations taken with multiple telescopes but not by the UV observations except for HD 102065 whose HI column density was measured with $E(B - V)$. The beam sizes (HPBW) of the 21-cm observations were $9.7' - 35'$ as listed in Table 3. To make correction

for the HI optical depth, we replaced N_{HI}^* in equation (8) by the present N_{HI} as

$$f_{\text{H}_2} = \frac{2N_{\text{H}_2}}{2N_{\text{H}_2} + N_{\text{HI}}}. \quad (9)$$

f_{H_2} at each point is typically reduced by 30 %–80 % from those in Gillmon et al. (2006) and Rachford et al. (2002), and the results are shown in Figure 16 and in Table 3. Figure 16 shows that molecular hydrogen is typically only 10^{-2} – 10^{-1} or less of the total in the column density regime, $N_{\text{HI}} \leq 1 \times 10^{21} \text{ cm}^{-2}$, whereas there are only a few observations for $N_{\text{HI}} > 10^{21} \text{ cm}^{-2}$.

It is worthwhile to note that the minimum HI column density is calculated from W_{HI} for the optically thin limit and is used to constrain the maximum f_{H_2} by assuming that equation (3) holds for H_2 . For instance, at a data point having $W_{\text{HI}} = 280 \text{ K km s}^{-1}$ and $\tau_{353} = 5.0 \times 10^{-6}$ in Figure 4 the minimum N_{HI} is calculated to be $5.1 \times 10^{20} \text{ cm}^{-2}$ by equation (1). This HI column density corresponds to $\tau_{353} = 2.4 \times 10^{-6}$ and the remaining $\tau_{353} = 2.6 \times 10^{-6}$ gives the possible contribution of H_2 at maximum when only neutral hydrogen either atomic or molecular forms are considered. The upper limit for f_{H_2} , $f_{\text{H}_2}(\text{upper limit})$, is then calculated to be 0.52. In this way, we have calculated $f_{\text{H}_2}(\text{upper limit})$ as a function of τ_{353} as shown in Figure 17. This provides a secure upper limit for f_{H_2} , because a mixture of HI and H_2 is more natural in the transition region between them, making the real f_{H_2} smaller than shown in Figure 17. Figure 17 shows $f_{\text{H}_2}(\text{upper limit})$ is typically ~ 0.5 , and the upper limit for the mass ratio of H_2 to HI is 58 % in $N_{\text{H}} = 10^{20} \text{ cm}^{-2}$ – 10^{22} cm^{-2} . For $N_{\text{H}} < 1 \times 10^{21} \text{ cm}^{-2}$ ($A_{\text{v}} < 0.5 \text{ mag}$), $f_{\text{H}_2}(\text{upper limit})$ is mostly less than 0.5 and the upper limit for the mass ratio of H_2 to HI is estimated to be 48 % on average. As such, H_2 is nearly equal to or less than HI in this regime with low extinction of $A_{\text{v}} < 0.5 \text{ mag}$. This is consistent with Figure 16, which indicates f_{H_2} is less than 10^{-2} – 10^{-1} . On the other hand, for $N_{\text{H}} > 1 \times 10^{21} \text{ cm}^{-2}$ ($A_{\text{v}} > 0.5 \text{ mag}$) $f_{\text{H}_2}(\text{upper limit})$ is 0.6 on average, suggesting that H_2 may dominate HI, whereas HI is still significant

at a level of at least 10 % of the total hydrogen. The upper limit for the mass ratio of HI to H₂ is estimated to be 64 % for $A_v > 0.5$ mag.

A recent study of the HI at high latitude concluded that additional column density is provided by H₂ and that the HI is not optically thick (Liszt 2014). This author found HI intensity decreases as found in the present work, but the author rejected T_s around 30 K for $E(B - V) \sim 0.1$ mag to explain the intensity decrease. $E(B - V) \sim 0.1$ mag corresponds to $6 \times 10^{20} \text{ cm}^{-2}$ in N_{HI} . This reasoning is not justified because T_s can be as low as 30 K even for $E(B - V) = 0.1$ mag as shown by theoretical calculations of T_s as a function of visual extinction in a model cloud (see e.g., Figure 2 of Goldsmith et al. 2007; also for more extensive calculations see Wolfire et al. 1995). The study by Liszt (2014) is therefore not justified as an counterargument for the optically thick HI. It is also to be considered that the timescale of H₂ formation is considerably larger than the timescale of the local ISM as described below.

We shall here discuss theoretical aspects of the HI-H₂ transition. The H₂ molecules are formed on the dust surface catalysis in the present-day universe and the H₂ formation timescale is given as $\sim 10 \cdot (n_{\text{HI}} [\text{cm}^{-3}]/100) \text{ Myr}$ (Hollenbach & Natta 1995). The current local clouds within 200 pc of the Sun have a crossing timescale of $\leq 1 \text{ Myr}$, which is too short to make H₂ as the major form by converting HI, suggesting that HI is generally overabundant relative to H₂. More detailed numerical simulations of H₂ formation from HI gas have been undertaken by incorporating the H₂ formation reaction from purely HI gas and it is shown for a density range of $10 \text{ cm}^{-3} - 10^3 \text{ cm}^{-3}$ that in $\sim 1 \text{ Myr}$ of cloud evolution the H₂ mass is about an order of magnitude smaller than the HI mass and that even in $\sim 10 \text{ Myr}$ the H₂ mass is still dominated by the HI mass (e.g., Inoue & Inutsuka 2012; Clark et al. 2012). It may be worthwhile to remark that Clark et al.’s paper presents “CO-free H₂”, but their results actually show that H₂ is a minor component, corresponding

to only ~ 0.1 of HI in mass (see their Figure 6). These results suggest that H_2 may not be the dominant form of the neutral hydrogen, while direct observations of H_2 to confirm this trend are not yet made at N_{H} larger than 10^{21} cm^{-2} .

The dark gas in the Milky Way is observationally identified in the local space outside the Galactic plane where the line of sight contamination is not significant (Grenier et al. 2005; *Planck* Collaboration et al. 2011). Therefore, the dark gas in the Milk Way is distributed within $\sim 200 \text{ pc}$ of the Sun in the Galactic latitude higher than 5° . Wolfire et al. (2010) presented numerical simulations of a giant molecular cloud with a lower density envelope and argued that an H_2 layer without CO surrounding a CO cloud may be significant in mass, providing a possible origin of the dark gas. The cloud size of a giant molecular cloud in Wolfire et al. (2010) is much larger than that of the local clouds, and the timescale for a giant molecular cloud is as large as a few 10 Myr (Fukui et al. 1999; Kawamura et al. 2009; Fukui & Kawamura 2010). These model simulations therefore do not apply to the local ISM having a much smaller timescale where the dark gas is identified. Recent Herschel observations of CII toward the disk clouds at $|b|$ less than 1° suggest that CO-free H_2 gas may be dominant in the disk outside the nearby regions analyzed in the present work (Langer et al. 2014). These observations also observed the giant molecular clouds that have ages of more than 10 Myr and they do not apply to the local dark gas either.

As a future direction an independent test of the HI optical depth and T_{s} is possible by using the HI absorption measurements toward extragalactic radio numerous continuum sources (Heiles & Troland 2003a,b; Dickey et al. 2003). We are able to extend this method to more continuum sources with a higher sensitivity and to compare the results with the present paper. Such measurements are also to be compared with numerical simulations of the HI- H_2 transition, allowing us to have a deeper insight into the H_2 formation and the

physical states of the hydrogen gas.

Another possibility which was not discussed in depth above is that the dust properties may be considerably different from the usual properties in the local space, as has been explored by the *Planck* collaboration (Planck Collaboration et al. 2014a). We shall defer to discuss this possibility until a full account of the *Planck* study is opened to the community.

5. Conclusions

We have carried out a study of the HI gas properties in the local ISM by using dust properties derived from the *Planck/IRAS* all sky survey at sub-mm/far-infrared wavelengths. The HI gas is in local regions within a few hundred pc of the Sun out of the Galactic plane, where giant molecular clouds do not exist. We find W_{HI} shows poor correlation with the sub-mm dust optical depth τ_{353} , whereas the correlation becomes significantly better if T_{d} , ranging from 13 K to 23 K, is analyzed in several small ranges of width 0.5 K. We hypothesize that the HI is optically thick and the saturation of the HI intensity is significant. We have shown that the HI emission associated with the highest T_{d} shows a good correlation expressed by a linear regression and hence derive a relationship, $W_{\text{HI}} = 1.15 \times 10^8 \cdot \tau_{353}$. An analysis of W_{HI} and N_{HI} based on coupled equations of radiative transfer and the HI optical depth yields both T_{s} and τ_{HI} . T_{s} is typically in the range from 15 K to 35 K and τ_{HI} from 0.5 to 3.0. The cold HI gas typically has density of $30 \text{ cm}^{-3} - 190 \text{ cm}^{-3}$, $N_{\text{HI}} = 5 \times 10^{20} \text{ cm}^{-2} - 3 \times 10^{21} \text{ cm}^{-2}$, and $\Delta V_{\text{HI}} \cong 15 \text{ km s}^{-1}$. We argue that the “dark gas” is explained by cold HI gas, which is 2–2.5 times more massive than the HI gas derived under the optically thin approximation. We consider two alternative interpretations: one is that H_2 is dominant instead of HI, and the other that variation of the dust opacity relative to the gas column density is significant. The fraction of H_2 f_{H_2} measured in the UV observations is consistent with that most of the hydrogen is atomic for

N_{H} less than $1 \times 10^{21} \text{ cm}^{-2}$, while for N_{H} larger than $1 \times 10^{21} \text{ cm}^{-2}$ UV observations are only a few, insufficient to constrain f_{H_2} . Minimum values of N_{HI} estimated by the optically thin limit constrain f_{H_2} to be less than ~ 0.5 , supporting that HI is at least comparable to H_2 . Theoretical studies of HI-cloud evolution indicate that f_{H_2} is less than 0.1 for $\sim 1 - \text{Myr}$ timescale by numerical simulations, lending support for that HI dominates H_2 at density $10 \text{ cm}^{-3} - 10^3 \text{ cm}^{-3}$ in the local interstellar medium. The second one the dust opacity variation is not reconciled with the general dust properties, either (equation 7).

T_{s} and τ_{HI} cannot be disentangled by HI intensity alone. This has been an obstacle in 21-cm HI astronomy. The *Planck* dust optical depth offers a potential tool to disentangle this issue for an ISM column density range $10^{20} \text{ cm}^{-2} - 10^{22} \text{ cm}^{-2}$. The opacity gives a measure of N_{HI} for given T_{d} , if CO is not detectable and the background HI gas is negligible. The present study suggests that the cold HI is dominant in the local ISM and such cold HI has important implications on related subjects, i.e., dust properties (in particular grain size evolution), the structure of molecular and atomic clouds, the interaction of HI with cosmic rays, and the derivation of the X_{CO} factor. These issues will be subjects to be pursued in follow-up studies.

We are grateful to John Dickey for his thoughtful comments and a valuable contribution on the HI properties. We are also grateful to Francois Boulanger and Jean-Phillippe Bernard for their initiative to begin the collaboration between the *Planck* and NANTEN2 teams. This work was financially supported by Grants-in-Aid for Scientific Research (KAKENHI) of Japanese society for the Promotion of Science (JSPS) (grant numbers 24224005, 25287035, 23403001, 23540277, and 23740149-01). This work was also financially supported by the Young Research Overseas Visits Program for Vitalizing Brain Circulation (R2211) and the Institutional Program for Young Researcher Overseas Visits (R29) by the Japan Society for the Promotion of Science (JSPS) and by the grant-in-aid for Nagoya

University Global COE Program, Quest for Fundamental Principles in the Universe: From Particles to the Solar System and the Cosmos,” from MEXT. We acknowledge the use of the Legacy Archive for Microwave Background Data Analysis (LAMBDA), part of the High Energy Astrophysics Science Archive Center (HEASARC). HEASARC/LAMBDA is a service of the Astrophysics Science Division at the NASA Goddard Space Flight Center. Some of the results in this paper have been derived using the HEALPix (Górski et al. 2005) package. We also utilize the data from Leiden/Argentine/Bonn Galactic HI Survey and from WHAM, VTSS and SHASSA, combined by D. Finkbeiner (2003) to form an all-sky composite $H\alpha$ map, and the Virginia Tech Spectral-Line Survey (VTSS), which is supported by the National Science Foundation, and the Southern H-Alpha Sky Survey Atlas (SHASSA), which is supported by the National Science Foundation. The Wisconsin H-Alpha Mapper is funded by the National Science Foundation.

REFERENCES

- Braun, R. 2012, *ApJ*, 749, 87
- Calabretta, M. R., Staveley-Smith, L., & Barnes, D. G. 2014, *PASA*, 31, 7
- Clark, P. C., Glover, S. C. O., Klessen, R. S., & Bonnell, I. A. 2012, *MNRAS*, 424, 2599
- Dame, T. M., Hartmann, D., & Thaddeus, P. 2001, *ApJ*, 547, 792
- Dickey, J. M. 2013, *Galactic Neutral Hydrogen*, ed. T. D. Oswalt & G. Gilmore, 549
- Dickey, J. M., & Lockman, F. J. 1990, *ARA&A*, 28, 215
- Dickey, J. M., McClure-Griffiths, N. M., Gaensler, B. M., & Green, A. J. 2003, *ApJ*, 585, 801
- Finkbeiner, D. P. 2003, *ApJS*, 146, 407
- Fukuda, T., Yoshiike, S., Sano, H., et al. 2014, *ApJ*, 788, 94
- Fukui, Y. 2013, in *Astrophysics and Space Science Proceedings*, Vol. 34, *Cosmic Rays in Star-Forming Environments*, ed. D. F. Torres & O. Reimer, 249
- Fukui, Y., & Kawamura, A. 2010, *ARA&A*, 48, 547
- Fukui, Y., Mizuno, N., Yamaguchi, R., et al. 1999, *PASJ*, 51, 745
- Fukui, Y., Sano, H., Sato, J., et al. 2012, *ApJ*, 746, 82
- Fukui, Y., Okamoto, R., Kaji, R., et al. 2014, *ApJ*, 796, 59, (Paper I)
- Gillmon, K., Shull, J. M., Tumlinson, J., & Danforth, C. 2006, *ApJ*, 636, 891
- Goldsmith, P. F., Li, D., & Krčo, M. 2007, *ApJ*, 654, 273

- Górski, K. M., Hivon, E., Banday, A. J., et al. 2005, *ApJ*, 622, 759
- Grenier, I. A., Casandjian, J.-M., & Terrier, R. 2005, *Science*, 307, 1292
- Heiles, C., & Troland, T. H. 2003a, *ApJS*, 145, 329
- . 2003b, *ApJ*, 586, 1067
- Hollenbach, D., & Natta, A. 1995, *ApJ*, 455, 133
- Inoue, T., & Inutsuka, S.-i. 2012, *ApJ*, 759, 35
- Kalberla, P. M. W., Burton, W. B., Hartmann, D., et al. 2005, *A&A*, 440, 775
- Kalberla, P. M. W., & Kerp, J. 2009, *ARA&A*, 47, 27
- Kawamura, A., Mizuno, Y., Minamidani, T., et al. 2009, *ApJS*, 184, 1
- Langer, W. D., Velusamy, T., Pineda, J. L., Willacy, K., & Goldsmith, P. F. 2014, *A&A*, 561, A122
- Liszt, H. 2014, *ApJ*, 783, 17
- Martin, P. G., Roy, A., Bontemps, S., et al. 2012, *ApJ*, 751, 28
- Mohan, R., Dwarakanath, K. S., & Srinivasan, G. 2004, *Journal of Astrophysics and Astronomy*, 25, 185
- Paradis, D., Dobashi, K., Shimoikura, T., et al. 2012, *A&A*, 543, A103
- Planck Collaboration, Abergel, A., Ade, P. A. R., et al. 2011, *A&A*, 536, A24
- . 2014a, *A&A*, 571, A11
- . 2014b, *A&A*, 566, A55

- Planck* Collaboration, Ade, P. A. R., Aghanim, N., et al. 2011, *A&A*, 536, A19
- Rachford, B. L., Snow, T. P., Tumlinson, J., et al. 2002, *ApJ*, 577, 221
- Rachford, B. L., Snow, T. P., Destree, J. D., et al. 2009, *ApJS*, 180, 125
- Reich, P., & Reich, W. 1986, *A&AS*, 63, 205
- Roy, A., Martin, P. G., Polychroni, D., et al. 2013, *ApJ*, 763, 55
- Strasser, S., & Taylor, A. R. 2004, *ApJ*, 603, 560
- Torii, K., Fukui, Y., Sano, H., et al. 2012, in *IAU Symposium*, Vol. 284, *IAU Symposium*, ed. R. J. Tuffs & C. C. Popescu, 389–392
- Wolfire, M. G., Hollenbach, D., & McKee, C. F. 2010, *ApJ*, 716, 1191
- Wolfire, M. G., Hollenbach, D., McKee, C. F., Tielens, A. G. G. M., & Bakes, E. L. O. 1995, *ApJ*, 443, 152
- Ysard, N., Abergel, A., Ristorcelli, I., et al. 2013, *A&A*, 559, A133

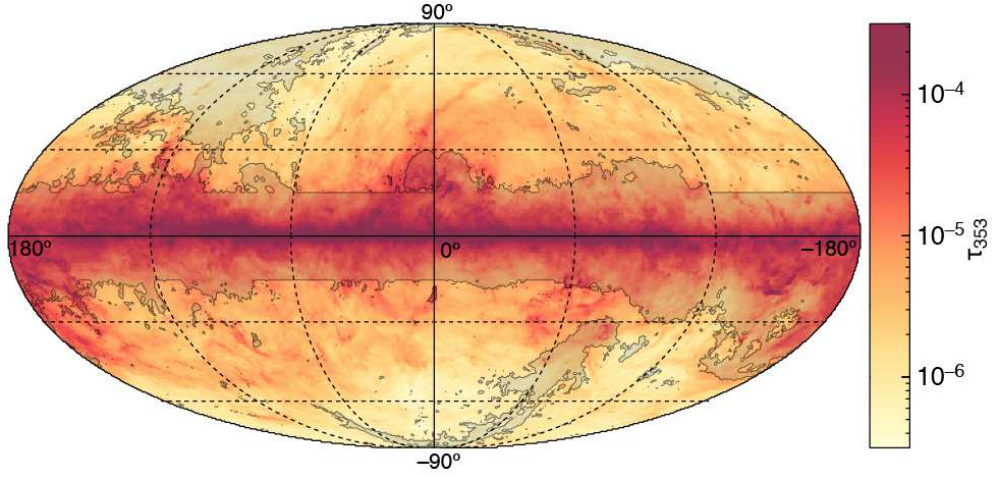


Fig. 1.— All-sky Mollweide projections of τ_{353} distribution in the galactic coordinate. The center of the map is $(l, b) = (0^\circ, 0^\circ)$, and the coverages of l and b are from -180° to $+180^\circ$ and from -90° to $+90^\circ$, respectively. Dashed lines are plotted every 60° in l and every 30° in b . The masked region used in the present analysis is shown by shading.

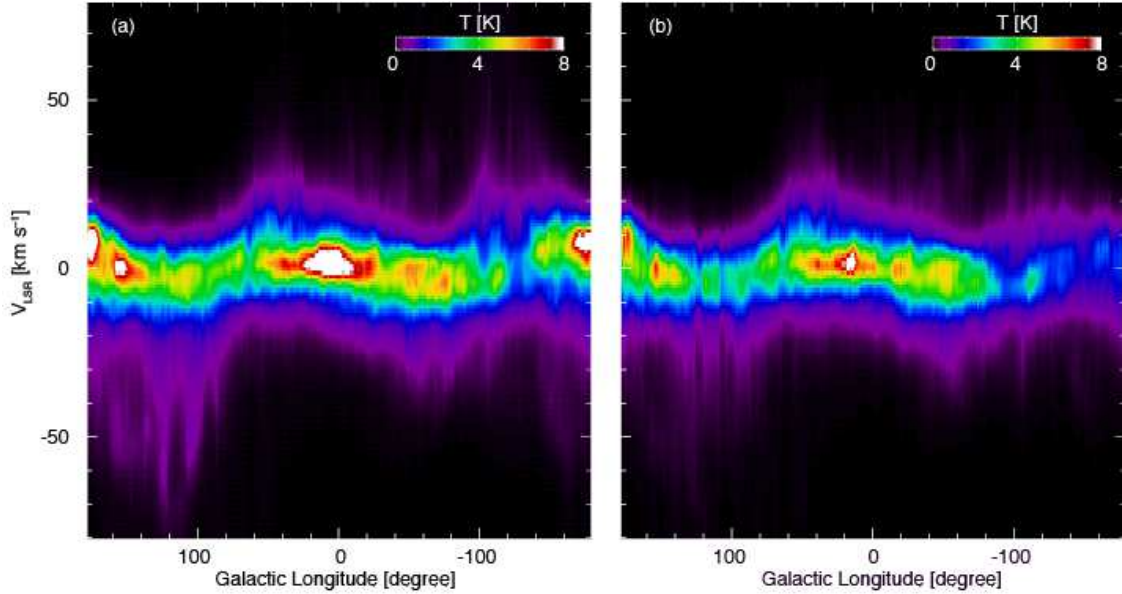


Fig. 2.— Longitude-velocity distributions of latitude averaged all-sky HI intensity after masking are shown. (See text in Section 2.2). (a) Criteria 1, 2, 4 and 5 are applied. (b) All the criteria are applied.

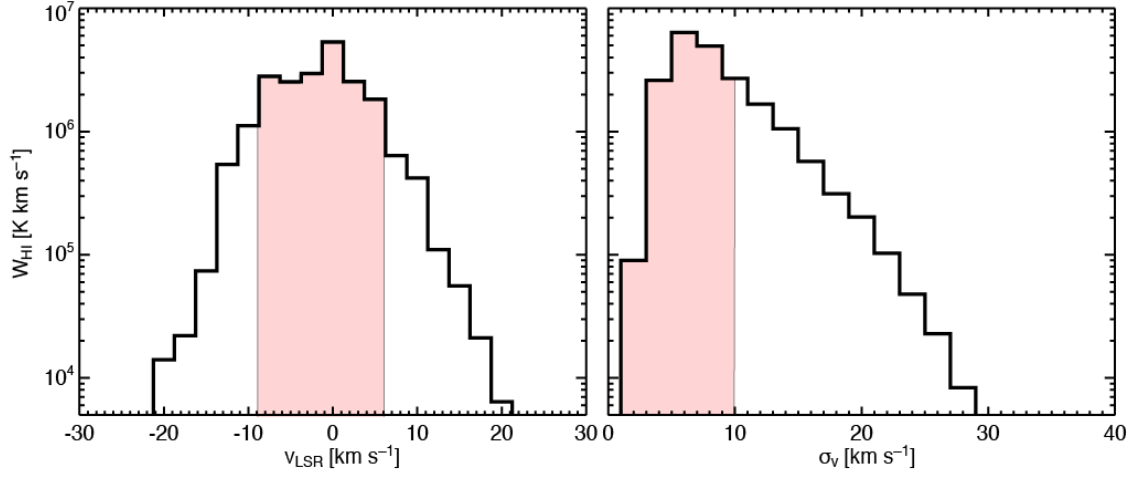


Fig. 3.— Intensity weighted histograms of (a) the peak velocity and (b) 1σ velocity dispersion, σ_v , of the HI emission shown in Figure 2(b). The shaded areas in (a) and (b) show the velocity ranges that account for 86 % and 81 % of W_{HI} , respectively.

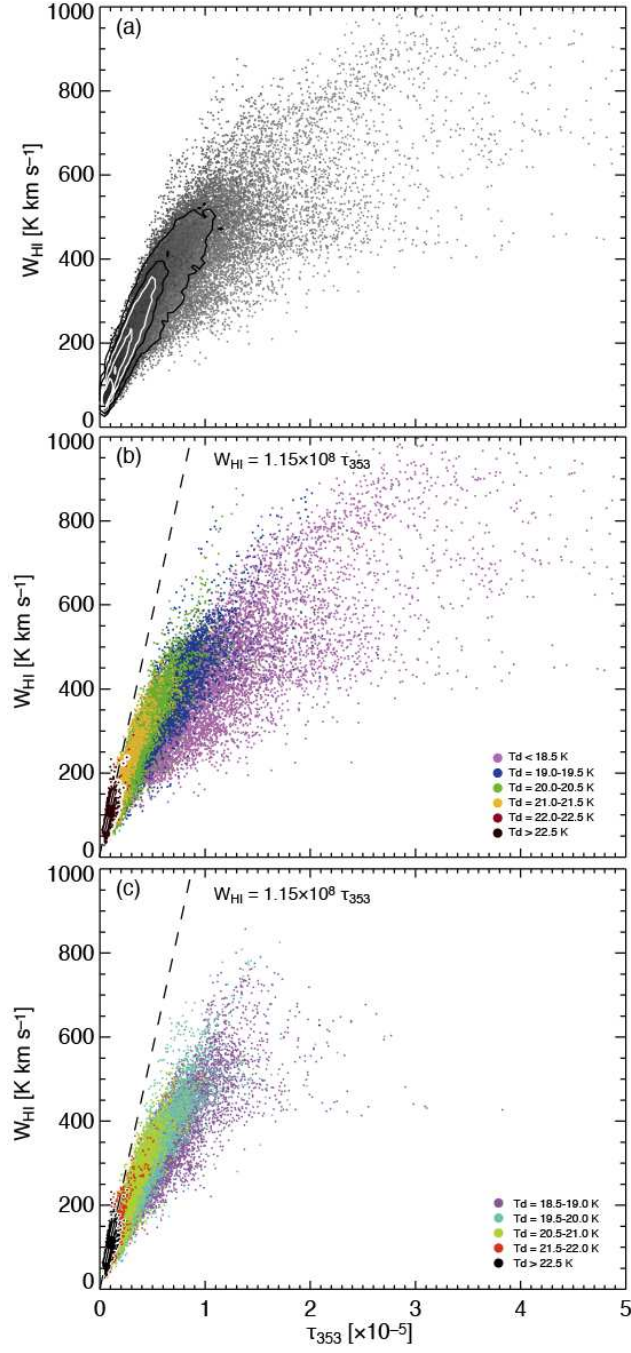


Fig. 4.— (a) Scatter plot between τ_{353} and W_{HI} . Contours are plotted at 1 %, 5 %, 10 %, 30 %, and 50 % of the peak. (b, c) The scatter plots of τ_{353} and W_{HI} for T_d in windows of 0.5 K interval every 1 K.

Table 1: Fitting results for k in Figure 4.

T_d [K]	N_{pixel}	Slope [K km s ⁻¹]	Intercept [K km s ⁻¹]	C.C.
(1)	(2)	(3)	(4)	(5)
< 18.5	9446	3.5×10^7	67.6	0.80
18.5–19.0	8327	5.1×10^7	27.9	0.85
19.0–19.5	12692	5.7×10^7	22.3	0.92
19.5–20.0	17233	6.4×10^7	13.8	0.93
20.0–20.5	17764	7.0×10^7	7.3	0.94
20.5–21.0	11299	7.7×10^7	4.1	0.94
21.0–21.5	5607	8.7×10^7	−1.3	0.93
21.5–22.0	3278	12.5×10^7	−14.3	0.88
22.0–22.5 [†]	1693	10.2×10^7	—	0.77
22.5 ≤ [†]	3278	11.5×10^7	—	0.70

Note. — Column (1): T_d range. (2) Number of pixels used for the fitting. (3, 4) Fitting results. (5) Correlation coefficients for the plot. [†] stands for the ranges in which intercept is fixed to be zero.

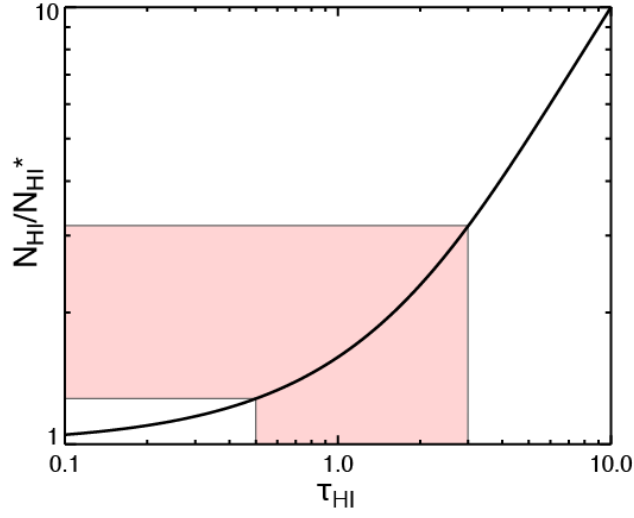


Fig. 5.— Curve of equation (5), $N_{\text{HI}}/N_{\text{HI}}^* = \tau_{\text{HI}}/[1 - \exp(-\tau_{\text{HI}})]$, is shown. The shaded area shows the typical τ_{HI} range of 0.5–3.0 determined in Figure 9(a), which correspond to $N_{\text{HI}}/N_{\text{HI}}^*$ of ~ 1.3 –3.1, respectively.

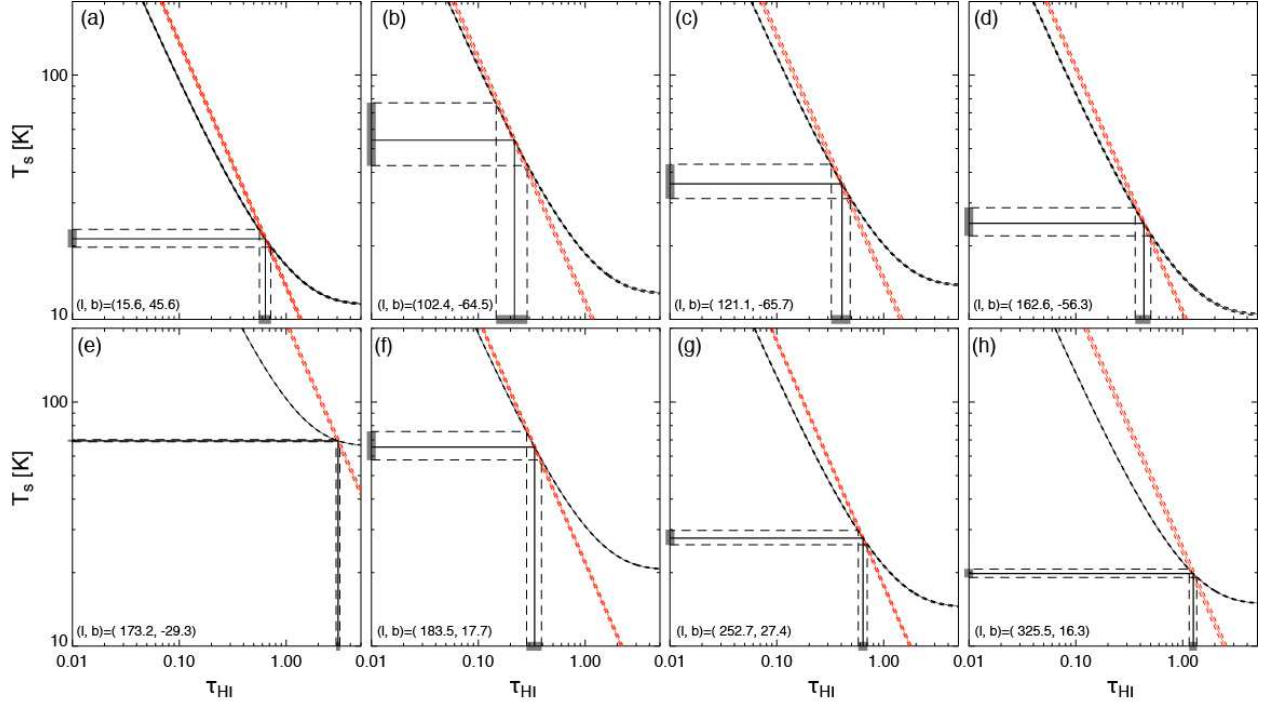


Fig. 6.— Examples for τ_{HI} and T_s estimates. Black line shows curves given by equation (4), while red line equation (6). Dotted lines show the error range of each curve, where the intrinsic observational errors in τ_{353} and W_{HI} are considered. The resulting errors for τ_{HI} and T_s are shown with thick line on the bottom and left axes of each panel.

Table 2: Derived τ_{HI} and T_s at the eight regions in Figure 6.

Region	l [$^\circ$]	b [$^\circ$]	τ_{353} [$\times 10^{-6}$]	T_d [K]	W_{HI} [K km s $^{-1}$]	N_{HI} [$\times 10^{20}$ cm $^{-2}$]	τ_{HI}	T_s [K]
(1)	(2)	(3)	(4)	(5)	(6)	(7)	(8)	(9)
a	15.6	45.6	2.4	20.6	179.3	5.1	$0.64^{+0.08}_{-0.08}$	21^{+2}_{-2}
b	102.4	−64.5	1.8	20.5	180.8	3.9	$0.25^{+0.11}_{-0.11}$	54^{+23}_{-12}
c	121.1	−65.7	2.3	20.3	197.5	4.7	$0.40^{+0.08}_{-0.08}$	36^{+7}_{-5}
d	162.6	−56.3	1.7	21.2	146.1	3.7	$0.43^{+0.07}_{-0.07}$	25^{+4}_{-3}
e	173.2	−29.3	2.7	17.6	930.0	5.7	$3.06^{+0.13}_{-0.12}$	69^{+1}_{-1}
f	183.4	17.7	5.1	19.8	375.4	6.3	$0.23^{+0.06}_{-0.06}$	69^{+23}_{-13}
g	252.7	27.4	3.3	21.0	250.1	6.8	$0.64^{+0.06}_{-0.06}$	28^{+2}_{-2}
h	325.5	16.3	6.8	20.4	386.7	14.3	$1.25^{+0.10}_{-0.11}$	20^{+1}_{-1}

Note. — Column (1): Name of region. (2, 3): Position in the galactic coordinate. (4–6): τ_{353} , T_d and W_{HI} of the target region. (7): HI column density without optically thin assumption. (8, 9): Derived τ_{HI} and T_s with errors.

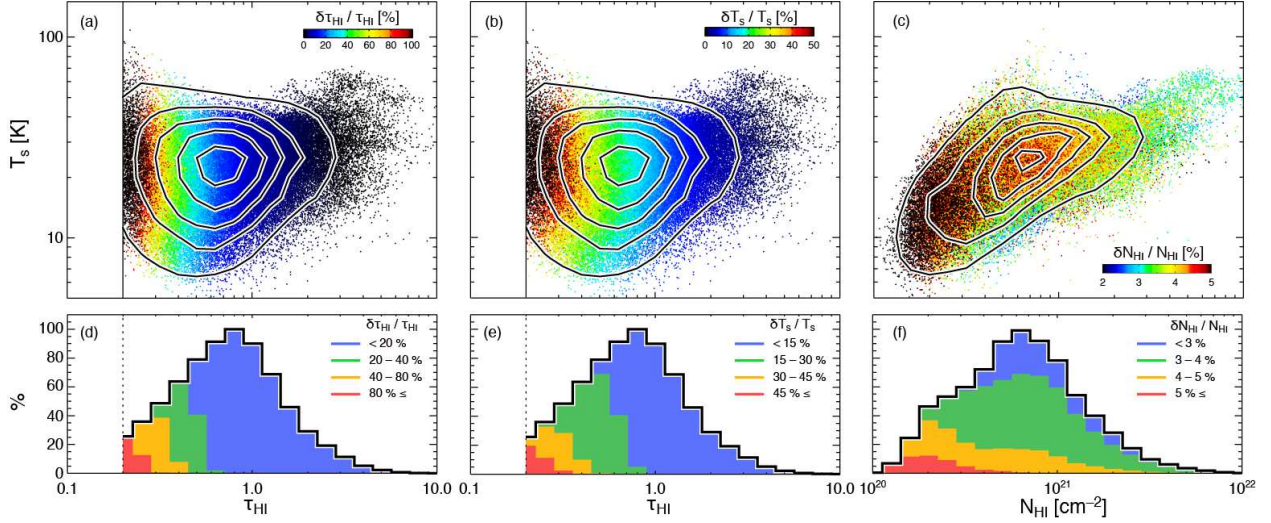


Fig. 7.— (a, b) Distributions of τ_{HI} and T_s , where color represents the fractional errors of (a) τ_{HI} and (b) T_s (in percent). The errors indicate the full lengths of the bars at 1σ levels in Figure 6. (c) Distributions of N_{HI} and T_s . Color represents the fractional 1σ error of N_{HI} . Contours show the 2D histograms and are plotted at 10 %, 30 %, 50 %, 70 %, and 90 % of the peaks. (d–f) Stacked histograms of τ_{HI} for various τ_{HI} and T_s error ranges, respectively. (f) Stacked histograms of N_{HI} for various N_{HI} error ranges. Each histogram in (d–e) is normalized at its peak.

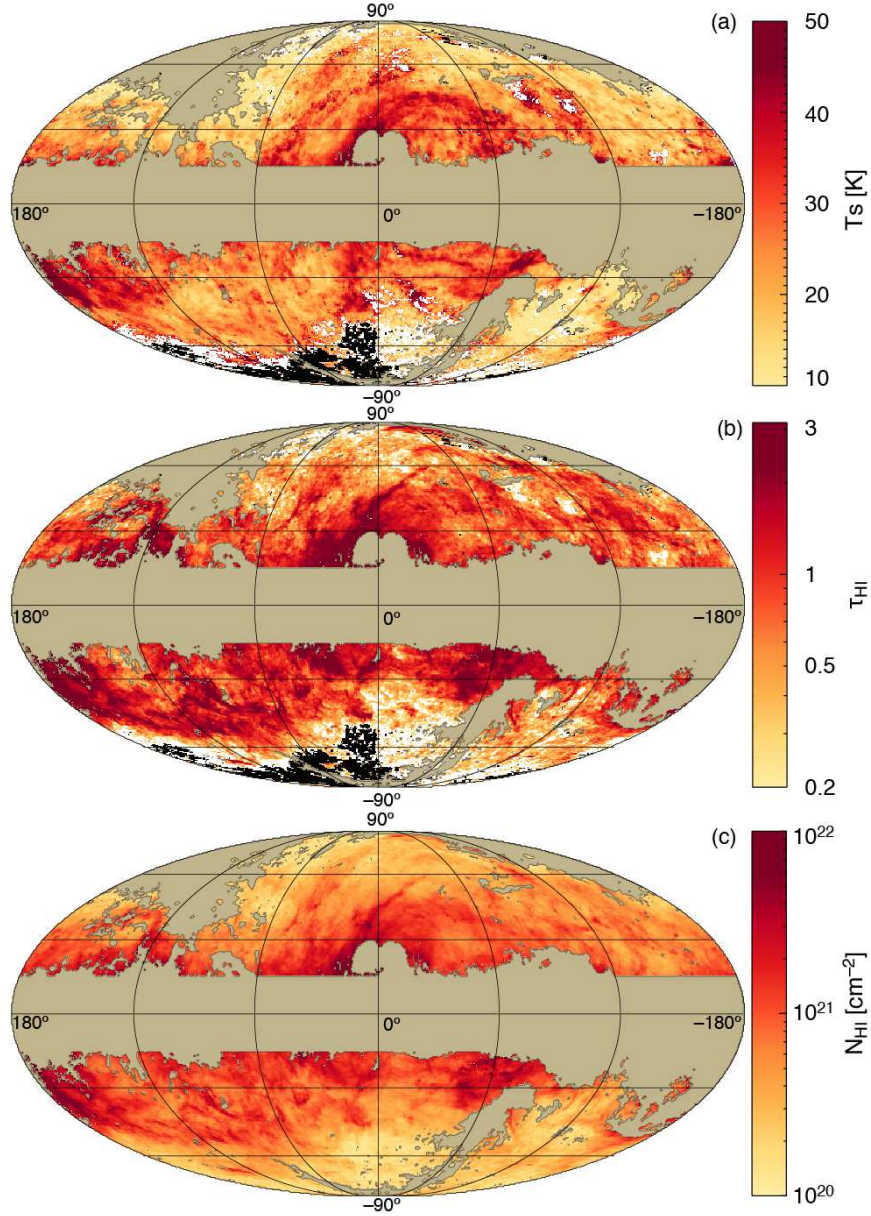


Fig. 8.— All-sky distributions of the (a) T_s and (b) τ_{HI} maps. The masked region is shown in gray. The black dots represent the region where $T_d > 22.5$ K. The white dots show the points where T_s and τ_{HI} are not determined because $\tau_{\text{HI}} < 0.2$. In (c) we use N_{HI}^* instead of N_{HI} for the points colored in white or black in (a) and (b). The center of the map is $(l, b) = (0^\circ, 0^\circ)$, and the coverages of l and b are from -180° to $+180^\circ$ and from -90° to $+90^\circ$, respectively. Dashed lines are plotted every 60° in l and every 30° in b .

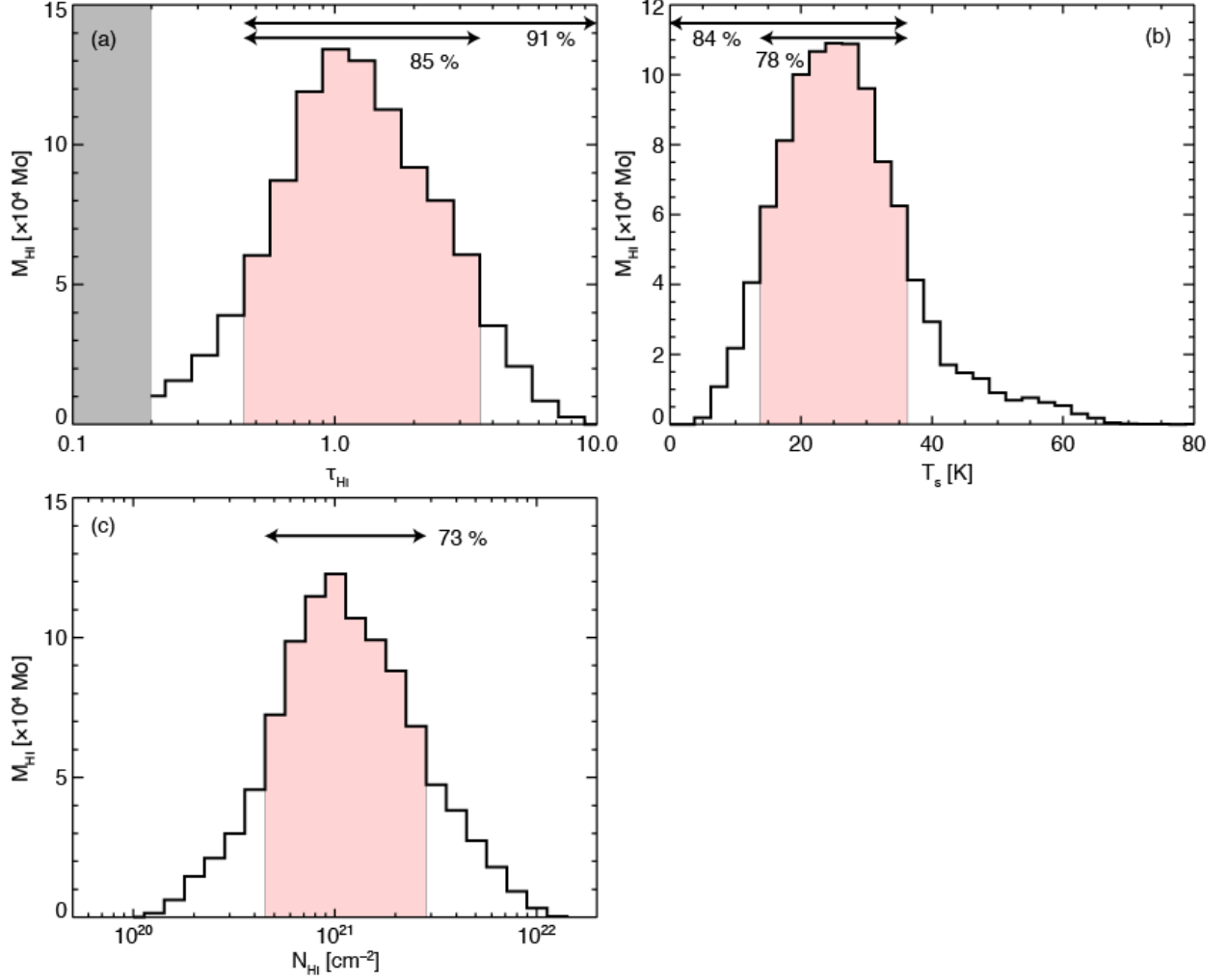


Fig. 9.— Histograms of (a) T_s , (b) τ_{HI} and (c) T_d weighted by HI mass, where distance is assumed to be 150 pc. The gray area in (a) indicates the lower limit of τ_{HI} . The area filled in pink in each panel is defined to contain about 70 %–80 % of the all points.

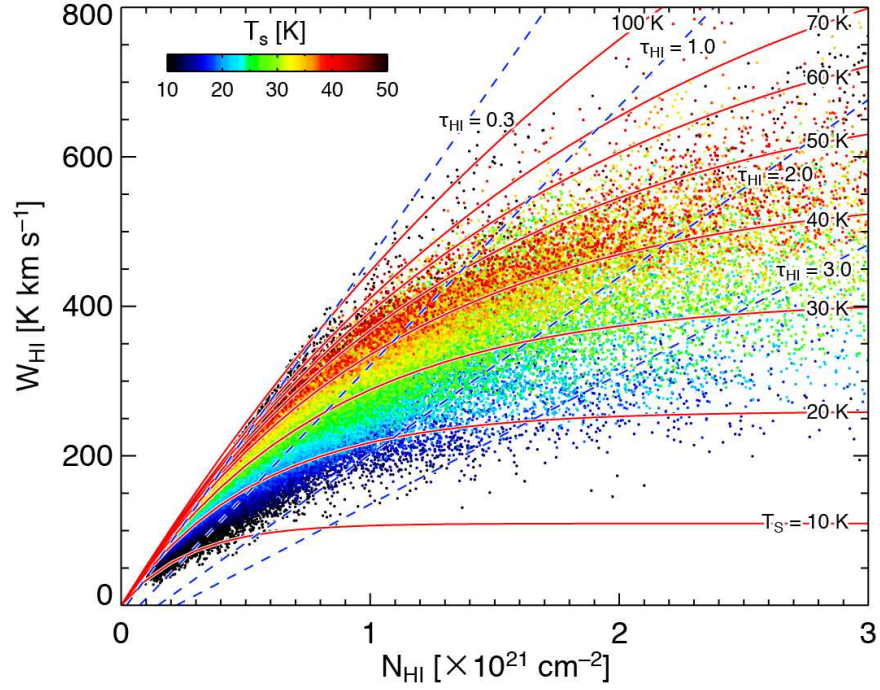


Fig. 10.— Correlation plot between W_{HI} and N_{HI} . Color represents T_s of each point. The dashed red lines and the dashed blue lines indicate W_{HI} derived with equations (4) and (6) for $T_s = 10\text{ K} - 100\text{ K}$ and for τ_{HI} , 0.3, 1.0, 2.0 and 3.0, respectively. Here ΔV in equations (4) and (6) is uniformly assumed to be 15 km s^{-1} .

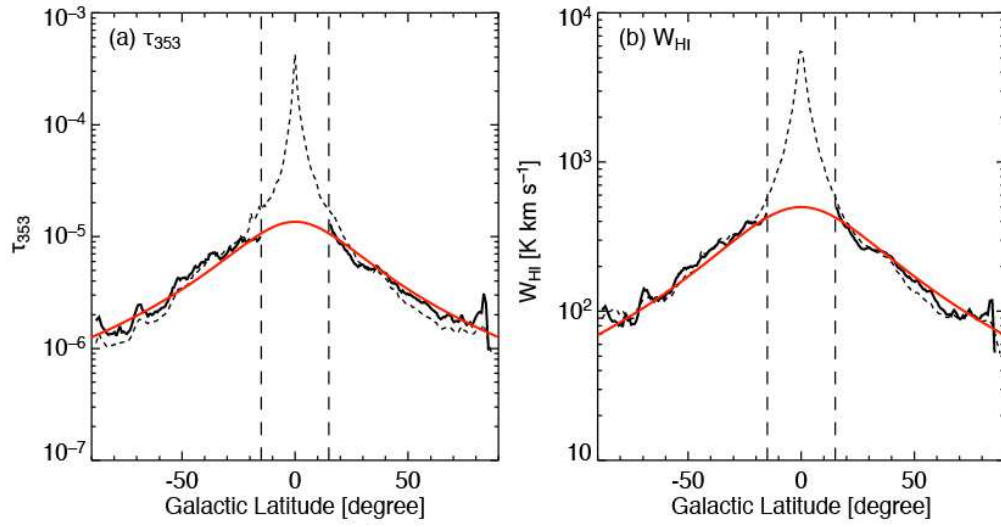


Fig. 11.— Curves of averaged (a) τ_{353} and (b) W_{HI} along the Galactic latitude with mask (black solid line) and without mask (black dotted line). Vertical dashed lines indicate $|b| = 15^\circ$. Red lines show the results of fitting with a Lorentzian function for the masked data. Half widths of the resulting curves are $28^\circ.8$ and $36^\circ.1$ for τ_{353} and W_{HI} , respectively.

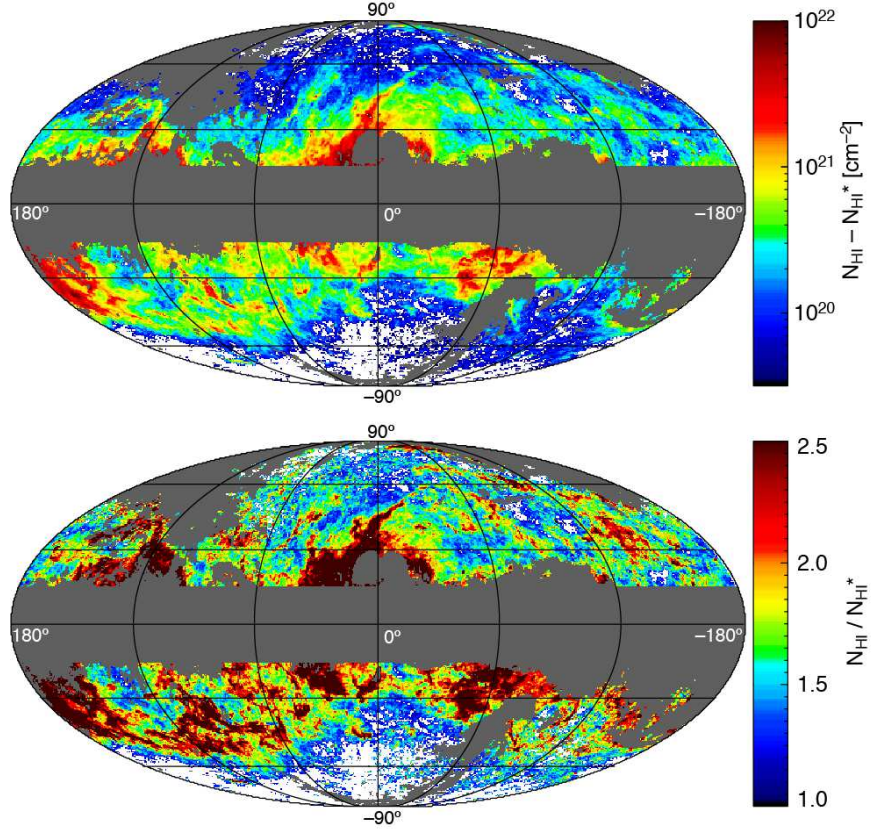


Fig. 12.— All-sky distributions of (a) the subtracted column density of the cold HI: $N_{\text{HI}} - N_{\text{HI}}^*$, and of (b) the ratio of N_{HI} to N_{HI}^* . The masked region is shown in gray, and the points where T_s and N_{HI} are not determined are shown in white. The center of the map is $(l, b) = (0^\circ, 0^\circ)$, and the coverages of l and b are from -180° to $+180^\circ$ and from -90° to $+90^\circ$, respectively. Dashed lines are plotted every 60° in l and every 30° in b .

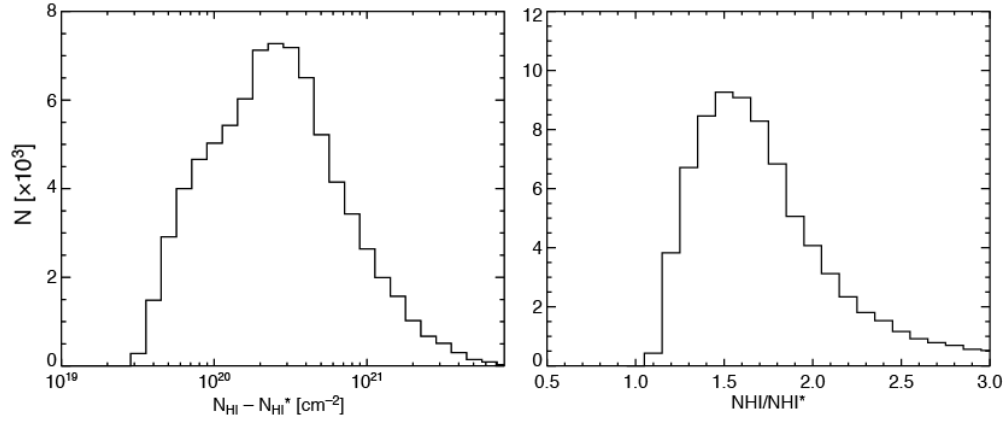


Fig. 13.— Histograms of (a) $N_{\text{HI}} - N_{\text{HI}^*}$ and (b) $N_{\text{HI}}/N_{\text{HI}^*}$ shown in Figure 12.

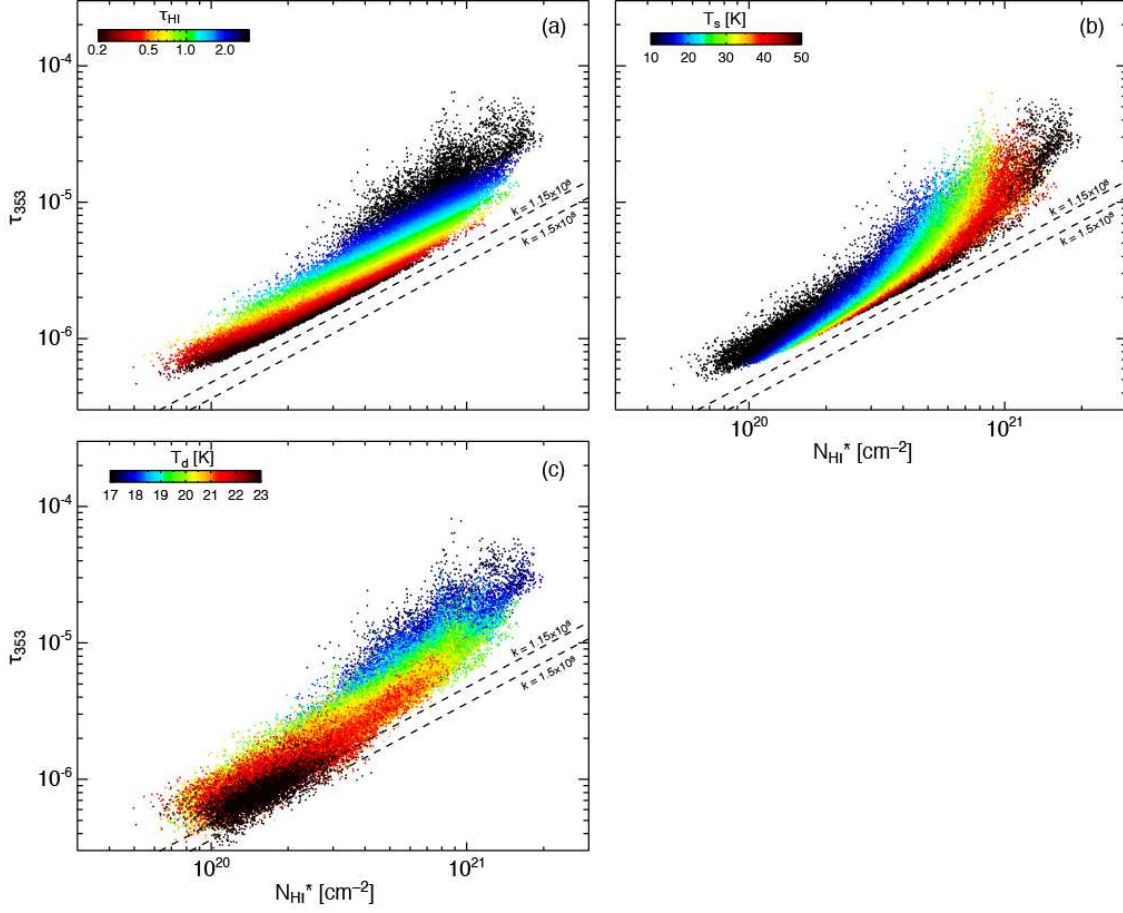


Fig. 14.— Scatter plots between N_{HI}^* and τ_{353} . Color represents τ_{HI} , T_s and T_d in the panels (a), (b) and (c), respectively. The dashed lines indicate the relations for $k = 1.15 \times 10^8$ K km s $^{-1}$ and 1.5×10^8 K km s $^{-1}$.

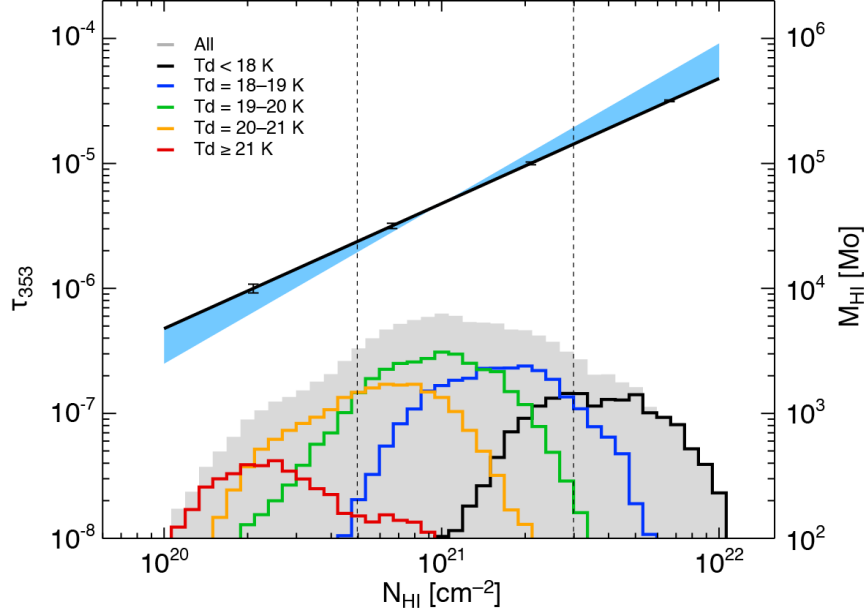


Fig. 15.— Correlation between N_{HI} and τ_{353} is shown by the thick line, where $N_{\text{HI}} = 2.1 \times 10^{26} \cdot \tau_{353}$. Representative values of the τ_{353} error are also plotted by bars. The area colored in light-blue shows variation of the correlation provided by equation 7 (See Section 4 for details). Histograms show N_{HI} weighted by the HI mass at various T_d : black ($T_d < 18$ K), blue ($18 \text{ K} \leq T_d < 19 \text{ K}$), green ($19 \text{ K} \leq T_d < 20 \text{ K}$), yellow ($20 \text{ K} \leq T_d < 21 \text{ K}$) and red ($21 \text{ K} \leq T_d$). Gray includes all points. Here vertical dashed lines indicate the range of typical N_{HI} defined in Figure 9(c).

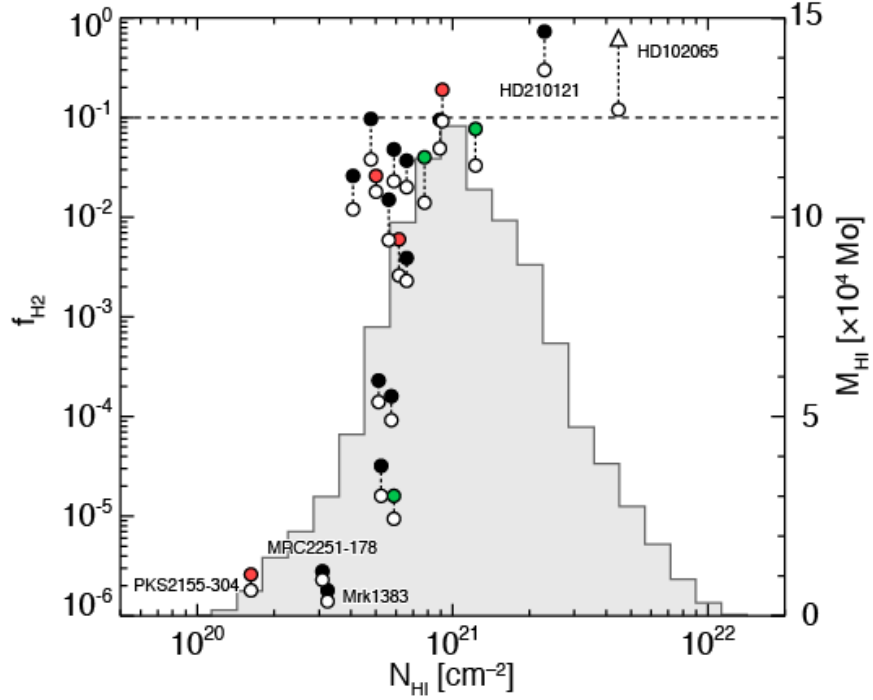


Fig. 16.— Plots of f_{H_2} for N_{HI} . Filled circles and open circles show f_{H_2} before and after τ_{HI} correction, respectively. The colors of the filled circles indicate different HPBW of the 21-cm observations used in the UV studies. The filled black circles indicate a HPBW of $21''$, and the green ones and the red ones have $9.7''$, and larger than $30''$, respectively. The open triangle indicates HD 102065, whose HI column density was directly measured with the $E(B - V)$ measurements without optically thin assumption (Rachford et al. 2002). Here the histogram of N_{HI} weighted by mass in Figure 9(c) is also shown.

Table 3: Parameters of the f_{H_2} estimates.

Target	(l , b)	Ref.	N_{H_2} [cm^{-2}]	N_{HI} [cm^{-2}]	HPBW [arcmin]	$f_{\text{H}_2}^*$	f_{H_2}
(1)	(2)	(3)	(4)	(5)	(6)	(7)	(8)
3C 249.1	(130° 39, 38° 55)	1	9.5×10^{18}	4.8×10^{20}	21	9.8×10^{-2}	2.4×10^{-2}
ESO 141-G55	(338° 18, −26° 71)	1	2.1×10^{19}	1.2×10^{21}	34	7.8×10^{-2}	3.6×10^{-2}
H1821+643	(94° 00, 27° 42)	1	8.1×10^{17}	6.2×10^{20}	9.7	6.0×10^{-3}	2.2×10^{-3}
HE 1143-1810	(281° 85, −41° 71)	1	3.5×10^{16}	5.1×10^{20}	21	2.3×10^{-4}	1.4×10^{-4}
MRC 2251-178	(46° 20, −61° 33)	1	3.5×10^{14}	3.1×10^{20}	21	2.8×10^{-6}	2.5×10^{-6}
Mrk 9	(158° 36, 28° 75)	1	2.3×10^{19}	9.0×10^{20}	21	9.5×10^{-2}	4.7×10^{-2}
Mrk 335	(108° 76, −41° 42)	1	6.8×10^{18}	5.9×10^{20}	21	4.8×10^{-2}	1.9×10^{-2}
Mrk 509	(35° 97, −29° 86)	1	7.4×10^{17}	6.5×10^{20}	21	3.9×10^{-3}	2.0×10^{-3}
Mrk 1383	(349° 22, 55° 12)	1	2.2×10^{14}	3.2×10^{20}	21	1.8×10^{-6}	1.5×10^{-6}
Mrk 1513	(63° 67, −29° 86)	1	2.6×10^{16}	5.7×10^{20}	21	1.6×10^{-4}	7.8×10^{-5}
MS 0700.7+6338	(152° 47, 25° 63)	1	5.6×10^{18}	7.7×10^{20}	35	4.0×10^{-2}	9.5×10^{-3}
NGC 7469	(83° 10, −45° 47)	1	4.7×10^{19}	9.2×10^{20}	9.7	1.9×10^{-1}	8.7×10^{-2}
PG 0804+761	(138° 28, 31° 03)	1	4.6×10^{18}	5.0×10^{20}	9.7	2.6×10^{-2}	2.1×10^{-2}
PG 0844+349	(188° 56, 37° 97)	1	1.7×10^{18}	5.6×10^{20}	21	1.5×10^{-2}	4.6×10^{-3}
PG 1211+143	(267° 55, 74° 32)	1	2.4×10^{18}	4.1×10^{20}	21	2.6×10^{-2}	7.3×10^{-3}
PG 1302-102	(308° 59, 52° 25)	1	4.2×10^{15}	5.3×10^{20}	21	3.2×10^{-5}	1.3×10^{-5}
PKS 0558-504	(257° 96, −28° 57)	1	2.8×10^{15}	5.9×10^{20}	34	1.6×10^{-5}	1.0×10^{-5}
PKS 2155-304	(17° 73, −52° 25)	1	1.5×10^{14}	1.6×10^{20}	34	2.6×10^{-6}	1.5×10^{-6}
VII Zw 118	(151° 36, 25° 99)	1	6.9×10^{18}	6.6×10^{20}	21	3.7×10^{-2}	1.9×10^{-2}
HD 102065 [†]	(300° 03, −18° 00)	2	3.2×10^{20}	4.5×10^{21}	—	$6.5 \times 10^{-1\dagger}$	1.2×10^{-1}
HD 210121	(56° 88, −44° 46)	2	5.6×10^{20}	2.3×10^{21}	36	7.2×10^{-1}	2.5×10^{-1}

Note. — Column (1): Name of target. (3): Reference number. 1: Gillmon et al. (2006), 2: Rachford et al. (2002). (4): N_{H_2} derived with the UV measurements. (5): N_{HI} obtained in the present study. (6) Beam size (HPBW) of the 21-cm observations used in the UV study. (7, 8) H_2 abundance ratios before and after τ_{HI} correction. [†] $E(B - V)$ was used to directly measure the HI column density without optically thin assumption in the literature.

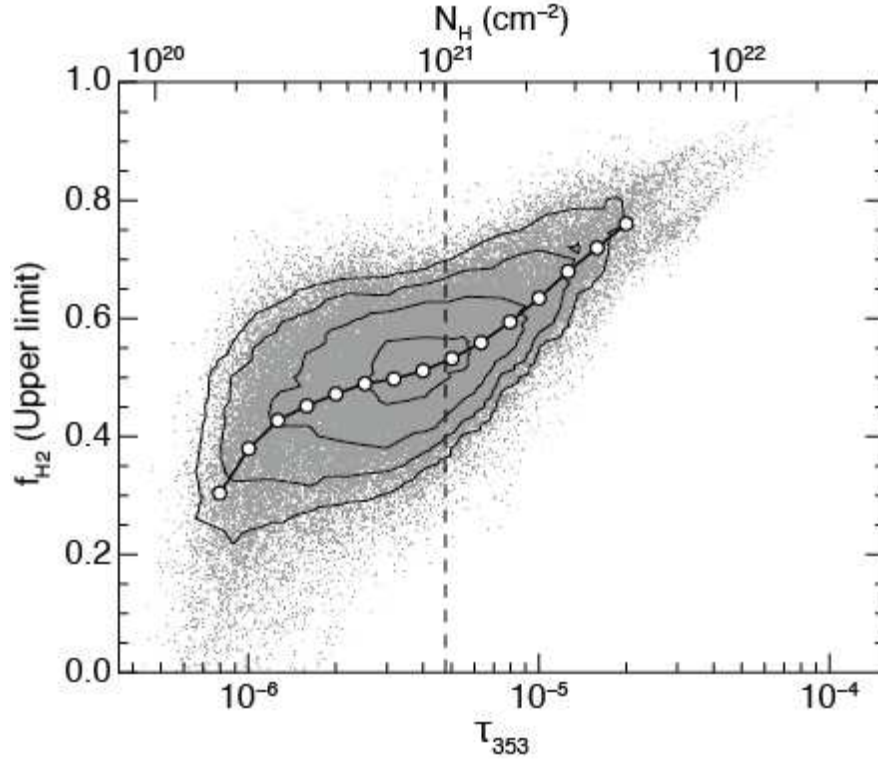


Fig. 17.— Scatter plots of f_{H_2} (upper limit) as a function of τ_{353} . White circles indicate the average value of f_{H_2} (upper limit) at each τ_{353} . Contours are plotted at 80 %, 40 %, 20 %, and 10 % of the peak, and the vertical line is plotted at $N_{\text{H}} = 1 \times 10^{21}$ cm⁻² ($A_{\text{v}} = 0.5$ mag).